Data-based hydrodynamic modelling of a fixed OWC wave energy converter

M. Rosati, T. Kelly, Demián G. Violini and J. V. Ringwood

***Abstract*—System identification (SI) techniques represent an alternative strategy to provide the hydrodynamic model of oscillating water column (OWC) devices, compared to relatively laborious, and potentially inaccurate, model determination from first principles. In particular, the assumption of small variations about equilibrium of the water column, combined with difficulties in calculating added mass, make the linear boundary-element modelling of OWCs particularly challenging. With SI, the parameters of the model are obtained, by minimizing a cost function, from input-output data. Even though OWC modelling typically features physics-based methods, such as linear potential theory or computational fluid dynamics (CFD), SI has already been successfully employed in the modelling of other wave energy devices. The main advantage of SI is its simplicity, as well as its potential validity range, where the dynamic model is valid over the range for which the identification data was recorded. This work aims to develop a data-based hydrodynamic model of a single chamber OWC wave energy converter by employing system identification. Real wave tank (RWT) data of a scaled model are gathered from the narrow tank experimental facility at Dundalk Institute of Technology (DkIT). Particular attention is paid to the selection of suitable input signals for the experimental campaign, in order to ensure that the model is subjected to the entire range of equivalent frequencies, and amplitudes, over which model validity is required.**

***Index Terms*—hydrodynamic modelling, oscillating water column, real wave tank, system identification, wave energy.**

I. Introduction

THE global wave energy potential has been estimated by different authors [1]–[3], who report around 16000 - 18500 TWh/year, and a slow variation rate, around 500 TWh/decade on average [3]. This makes wave energy a significant and relatively constant source of renewable energy.

Wave energy converters (WECs) harness the wave power, and one of the most promising devices is the so-called oscillating water column (OWC), depicted in Fig. 1. Its simplicity of operation and the presence of few moving components, all located above the water level, are the main advantages of OWCs. The motion of a water column, excited by incident waves, alternatively compresses and decompresses an air volume contained inside a pneumatic chamber. The chamber is connected to the atmosphere and, as a result, a bidirectional air flow is generated. A power-take-off (PTO) mechanism, namely a self-rectifying air turbine directly coupled with an electric generator, converts pneumatic energy to electricity, which is finally transferred to the power grid. A comprehensive review of OWC devices and air turbines is provided in [4]. Currently, besides the high production and operational costs, the commercial development of OWCs is hindered because of the lack of an efficient control system, and, in relation to this, it is imperative to note that the control problem is intrinsically characterized by modelling-related assumptions and requirements.

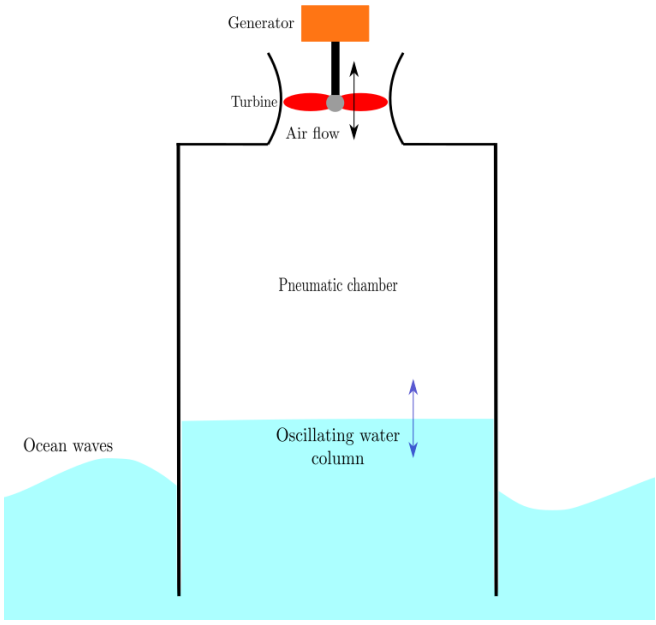

Fig. 1. Schematic representation of an OWC.

System identification (SI) techniques [5] represent an alternative strategy to provide the hydrodynamic model of OWC devices, compared to the laborious process of model determination from first principles, in which, as a consequence of linear potential theory (LPT) assumptions, the model is linearised around its equilibrium point. In contrast to LPT, the main advantage of SI, besides its simplicity, is its validity range, meaning that the dynamic model is valid over the range for which the identification data have been recorded. Ultimately, SI is a data-based modelling approach in which the parameters of the model are obtained from input-output data by minimizing a cost function, related to the model fidelity. SI models can

This paper is based upon work supported by Science Foundation Ireland under Grant No. 12/RC/2302_P2 for the Marine and Renewable Energy Ireland (MaREI) centre and under Grant no. 13/IA/1886.

M. Rosati is a member of COER (Centre for Ocean Energy Research), Maynooth University, Maynooth, Co. Kildare, Ireland (e-mail: marco.rosati.2021@mumail.ie).

T. Kelly is at Dundalk Institute of Technology (DkIT), Dundalk , Co. Louth, Ireland (e-mail: thomas.kelly@dkit.ie).

Demián G. Violini is at University of Quilmes, Bernal, Provincia de Buenos Aires, Argentina (e-mail: ddgv83@gmail.com).

J. V. Ringwood is the director of COER (Centre for Ocean Energy Research), Maynooth University, Maynooth, Co. Kildare, Ireland (e-mail: john.ringwood@mu.ie).

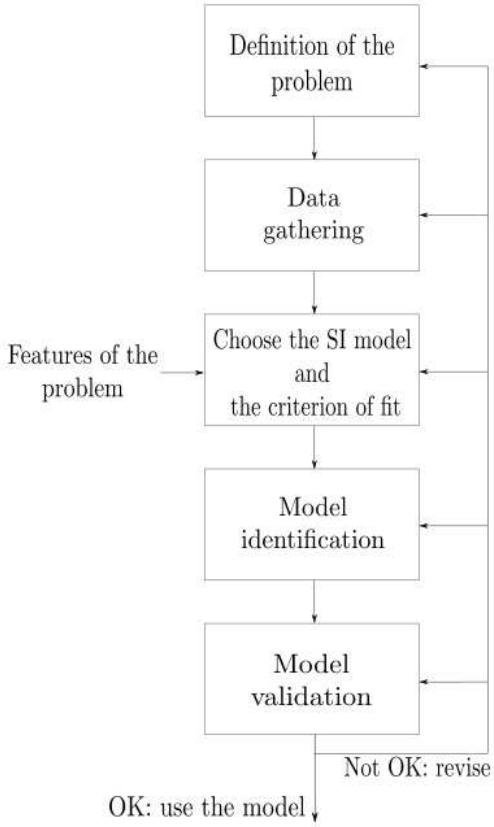

Fig. 2. Schematic representation of the SI loop.

be solely based on data (black-box models), or else can make use of some physics-based information (grey-box models) [6]. In either case, a suitable model and a fitting criterion, which is needed in order to evaluate the performance of the model, have to be chosen. The parameters of the model are then identified by feeding a numerical optimization algorithm with training, or identification, data. Finally, the model is validated against a separate set of validation data, meaning that the capacity of the model to predict the behaviour of the device, while working with a different data set, is assessed. This procedure is summarized by the loop shown in Fig. 2. An essential aspect to keep in mind is that the validation data must be different from those employed during the identification. Moreover, it has to be noted that the choice of suitable input signal is of primary importance for the parametric model to perform well in the real sea environment. The range of frequencies, and amplitudes, of the input signals employed in the training phase should correspond to the range of equivalent frequencies, and amplitudes, over which model validity is required.

Even if the application of SI in wave energy is relatively recent, SI has already been successfully employed in WEC modelling [7]–[10]. In two joint publications [7], [8], SI is used in order to derive a force-to-position model, with a force being the PTO force, and a wave-to-position model of a WEC by using three discrete time parametric structures. Two of the three model structures, namely the autoregressive with exogenous input (ARX) model and the Kolmogorov-Gabor polynomial (KGP) model, are linear in the parameters, whereas the multi-layer perceptron (MLP) artificial neural network (ANN), is nonlinear. The data are gathered from numerical wave tank (NWT) experiments, which are built by means of an open source computational fluid dynamics (CFD) software. In [9], the wave-to-force and the force-to-position models of a WEC are identified, in the frequency domain, by using a linear black-box model, and a nonlinear Hammerstain-Wiener model. Note that the output in the wave-to-force model is the excitation force, whereas the input in the force-to-position model is the PTO force. In a recent paper [10], a linear force-to-position model for a three-body hinged-barge WEC is identified by using real wave tank (RWT) data and, similarly to the previous cases, the input is the PTO force. The authors identify a parametric model for the transfer function (TF) of the system by following three different strategies. The first approach is carried out in the frequency domain, whereas the other two utilize time domain identification techniques.

Fig. 3. Schematic representation of the model considered in this work.

In this work, system identification is employed in order to model an OWC device and derive a linear black-box model (Fig. 3), which is somewhat similar to the wave-to-position model sought in [7], [8]. Nonlinear SI models are not considered, since the results reported in [7]–[9] have shown no significant improvements with respect to linear models. On the left side of Fig. 3, the input of the model is the free surface elevation (FSE), namely the water elevation associated with an undisturbed (by a device) wave. On the right side of Fig. 3, the output of the model is the height of the water column measured at its centroid. In other words, the wave-to-position model in Fig. 3 is a mapping between FSE and the displacement of the water column. To this end, the time traces of the free surface elevation, $\eta(t)$, and the water column displacement, $y(t)$, are recorded and sampled during RWT experiments, where a scaled fixed OWC model is tested in irregular waves (IWs) and in regular waves (RWs). The two data sets are then separately employed in order to derive separate models of the type depicted in Fig. 3. Despite the fact that, normally, regular wave analysis precedes irregular wave analysis, in this work the order has been reversed, due to the fact that regular wave case is somewhat more complex, due to the absence of knowledge of some key parameters, namely $\eta(t)$. Therefore, this work focuses on the irregular wave case as the central focus of the system identification procedure, with the regular wave case mainly providing a source of model validation. In the literature, a somewhat diametrically opposite work is carried out in [11], where an OWC model is derived from first principles and tested against RWT data collected from an OWC device subjected to regular and irregular waves.

The remaining of this paper is organised as follow.

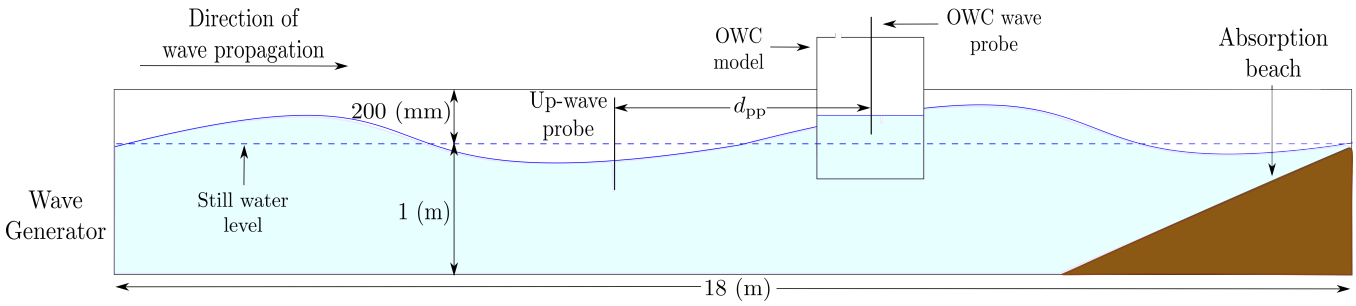

Fig. 4. Schematic representation of the narrow tank at DkIT.

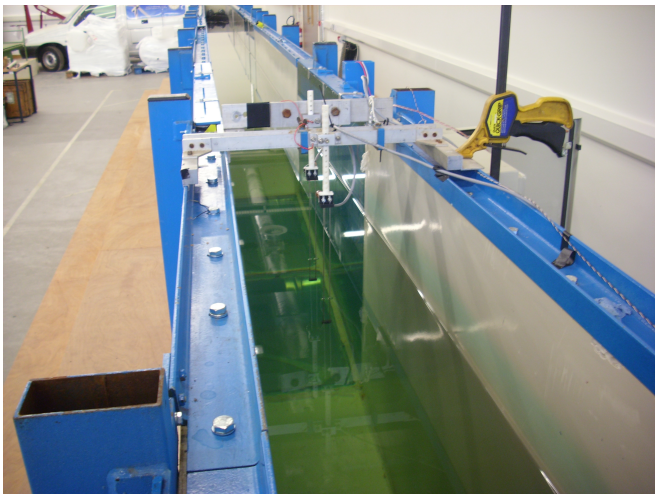

Fig. 5. Narrow tank at DkIT.

Section II contains the details about the testing facility and the experimental campaign. In section III, the parametric models for the irregular wave case are identified and validated. Section IV is dedicated to data-based modelling in the regular wave case. In section V, the models for the irregular and regular waves are briefly discussed. Finally, conclusions are drawn in section VI.

II. Real wave tank data gathering

A. Testing facility

The narrow tank (Fig. 5) at Dundalk Institute of Technology (DkIT), schematically illustrated in Fig. 4, is used in order to gather the RWT experimental data. On the left side of Fig. 4, the tank is equipped with a flap-type wave generator. On the right side, an absorption beach is positioned in order to minimise wave reflections from the beach towards the model. Since there is only one direction of wave propagation, the wave motion is basically two-dimensional. The tank has a length of 18 m, a width of 350 mm, a depth of 1 m, a freeboard of 200 mm and a probe-to-probe distance, d_{pp} (Fig. 4), of approximately 3 m, even though its precise value is unknown. During an experimental run, the displacement of the water column, $y(t)$, is recorded at its centroid by means of a wave probe, as shown in Fig. 4. In order to record the FSE, $\eta(t)$, at the same location where $y(t)$ is measured, the experiment has to be identically repeated in the absence of the OWC model in the tank. Particular attention has been paid in order to ensure that $\eta(t)$ (for the absent OWC case) and $y(t)$ are measured at the same location. Furthermore, it should be noted that the acquisition system and the wave maker are entirely isolated from each other, hence the data acquisition and the generation of excitation waves do not start at the same moment. Therefore, before using the data for OWC modelling, the time traces of the input need to be temporarily aligned with those of the output. To this end, the FSE measurements gathered from the up-wave probe (Fig. 4) during the two experiments are cross-correlated in order to estimate the time delay. The capability of the tank to reproduce a pseudo-random wave elevation time series, i.e. the tank repeatability, has already been assessed in previous work [12]. The 1:50 scaled fixed OWC model is made in marine plywood and scaled in accordance with Froude scaling [13]. The internal width of the chamber, equal to the width of the water column, is 288 mm. An iris valve, which simulates the effect of a turbine by creating an orifice with a variable diameter, is mounted at the top of the pneumatic chamber, and the diameter of its pupil is set, for the purpose of this work, at 30 mm.

In general, in any OWC model, the air spring effect due to air compressibility does not scale correctly if the air volume is scaled geometrically, i.e. scaled by the cube of the scaling factor. This implies that, when the pneumatic chamber is relatively small, the effects of air compressibility are usually negligible. In [14], the effects of air compressibility in OWCs are discussed and three possible thermodynamic models are analysed and compared. Furthermore, despite the fact that the behaviour of an oscillating water column can be quite complex, the water column mainly displaces vertically as a piston. This piston-like mode of motion is known as the pumping mode, which is also the main mode responsible for power production in OWC devices. Ultimately, in this work, the effects of air compressibility are neglected because the air volume is relatively small and, moreover, the pumping mode is assumed to be the only active mode of the water column.

A more comprehensive description of the narrow tank and the OWC model can be found in [13].

B. Experimental campaign

During the experimental campaign, the OWC model is tested under irregular and regular waves, so, ultimately, two separate data sets are collected. The time traces of the water column displacement, $y(k)$, and the

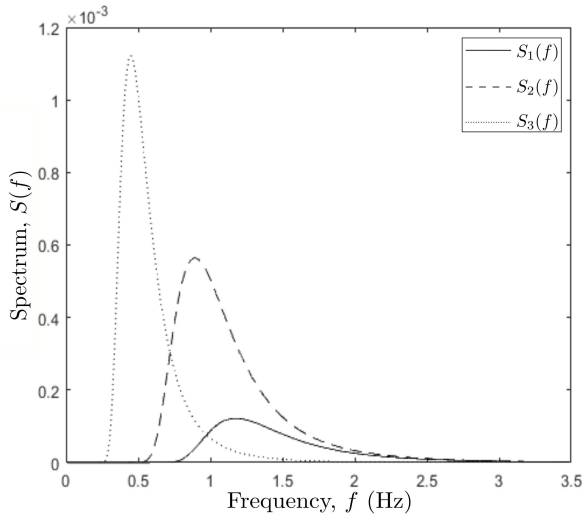

Fig. 6. Bretschneider spectra.

TABLE I
BRETSCHNEIDER SPECTRA

$S_i(f)$	T_e (s)	H_s (mm)
$S_1(f)$	0.85	4
$S_2(f)$	1.12	75
$S_3(f)$	2.23	75

free surface elevation, $\eta(k)$, are sampled and recorded over time instants, k, by means of the National Instrument LabVIEW software.

1) Irregular waves: The data collected during the experiments in irregular waves comprise three sets of input-output data, which have been originally generated in a previous study [15]. The OWC model is tested under three sea states, which correspond to different Bretschneider spectra (Fig. 6), named $S_1(f)$, $S_2(f)$ and $S_3(f)$. The wave maker utilises an inbuilt function in order to generate a time sequence of waves, whose spectrum matches the target Bretschneider spectrum. A generic Bretschneider spectrum can be expressed as a function of the frequency, f, as:

$$S_i(f) = \frac{5}{16} H_s^2 \frac{f^{-5}}{T_e^4} exp\left[-\frac{5}{4}(T_e f)^{-4}\right], \quad i = 1, 2, 3. \quad (1)$$

Table I reports the mean period, T_e, and the significant wave height, H_s, of the three spectra employed in this work. For each spectrum, $y(k)$ is recorded for 30 minutes and sampled at a frequency of acquisition, F_s, of 128 Hz. Then, after removing the OWC model from the wave tank, the experiment is identically repeated in order to separately record $\eta(k)$ where the OWC was positioned. For the sake of simplicity, the three sets of input-output data, which are recorded during the experiments with the spectra $S_1(f)$, $S_2(f)$ and $S_3(f)$, are respectively called D_1, D_2 and D_3. Note that each spectrum covers a different range of frequencies, and amplitudes, over which the OWC device is tested. The most significant spectrum is $S_3(f)$ because, in this case, the frequencies of the exciting waves lie within the resonant band of the pumping mode, which is the frequency band in which the uncontrolled device is designed to operate, in order to maximise power extraction [16], [17]. However, it is worth providing an insight into the behaviour of the device over the frequency range of $S_2(f)$ and $S_3(f)$, since a hypothetical control system may change the frequency band in which the device optimally operates.

2) Regular waves: As for the irregular wave case, the experiments in regular waves have been conducted as part of previous work [13], where the OWC model has been tested under different monochromatic waves. To this end, the wave maker generates a sequence of identical waves, meaning that they all have the same frequency and amplitude, of the type:

$$A_w cos(\omega t + \phi). \quad (2)$$

In equation (2), A_w is the wave amplitude in meters, ϕ is the phase of the wave in radians and $\omega = 2\pi f$ is the angular frequency in rad/s. Each experiment runs until reaching steady-state conditions, then $y(k)$ is recorded for 90 seconds with F_s = 32 Hz. Ultimately, sixty different regular wave trains, given by the combination of six amplitudes and ten frequencies, are tested. The amplitudes range from 5 to 30 mm with increments of 5 mm, whereas the range of frequencies spans from 0.4 to 1.3 Hz with increments of 0.1 Hz. Note that, in the regular wave case, the time traces of the FSE, $\eta(k)$, have not been recorded. However, in spite of the fact that knowledge of the empirical input data is incomplete, the amplitude, A_w, and frequency, f, of the tested monochromatic waves are known. This information is sufficient in order to establish a modelling procedure for the regular wave case.

III. SYSTEM IDENTIFICATION IN IRREGULAR WAVES

A. Methodology

In the irregular wave case, SI is carried out by following two distinct approaches, which are schematically represented in Fig. 7. In both cases, a linear polynomial ARX model, whose unknown parameters are a_i and b_i, is chosen as the SI model:

$$y(k) = -\sum_{i=1}^{n_a} a_i y(k-i) + \sum_{i=0}^{n_b} b_i u(k-n_d-i). \quad (3)$$

In equation (3), $y(k)$ and $u(k)$ are the k-th samples of the output and input respectively, the terms n_a and n_b are the orders of the ARX model, with n_d the input delay. In this work, the values of n_a, n_b and n_d are determined from a procedure described later on in this section. The number of unknowns in the ARX model of equation (3) is $n_a + n_b + 1$.

In order to compare the performance of the models in the identification and validation phases, the normalized root mean squared error (NRMSE) is chosen as the error metric:

$$NRMSE = \sqrt{\frac{\sum_k |y(k) - \hat{y}(k)|^2}{\sum_k |y(k)|^2}}, \quad (4)$$

where $y(k)$ is the measured value of the output, and $\hat{y}(k)$ is the model prediction.

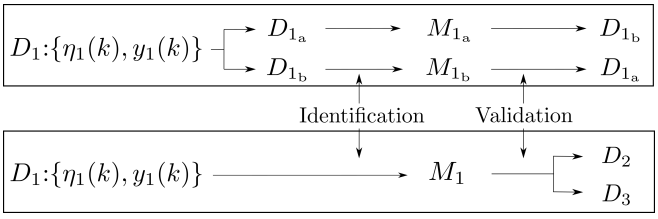

Fig. 7. First approach (above) and second approach (below) for the data set D_1.

In order to determine the orders n_a, n_b and n_d, a sequence of systematic trials, with incremental changes in n_a, n_b and n_d, has been implemented. At the end of each trial, the performance of the model is evaluated on the basis of the NRMSE. As already stated, the number of unknowns depends on the model orders and, generally, the NRMSE decreases as the number of model parameters increases. Therefore, a trade-off between model accuracy and model complexity has to be made; hence, to this end, the principle of parsimony is adopted. This principle potentially helps to set the variables in order to find a "parsimonious model", which is a model whose complexity ideally matches the problem complexity. To this end, consideration will be given to the complexity of the solution (in terms of the number of model parameters), as well as the model error metric, in the spirit of [18]. Ultimately, in this work, $n_a = 4$, $n_b = 2$ and the value of the input delay is set equal to -4. Note that a negative value of n_d implies that the ARX model is noncausal, meaning that both past and future values of the input are utilized in order to predict the output value, $y(k)$. In contrast, if $n_d > 0$, the ARX model is causal, where the output prediction only relies on past values of the input. Herein, the choice of a negative value for n_d is justified by the fact that, due to pressure wave propagation phenomena, the relationship between $\eta(k)$ and $y(k)$ is noncausal. Indeed, since pressure waves propagate faster than ocean waves, the device can somewhat perceive the presence of an incoming excitation wave in advance.

The unknown parameters of the ARX model, a_i and b_i, are found by solving a relatively simple least-squares optimization problem, which is derived, by applying some formulae (as done in [5], [8]), from equation (3).

1) First approach: The input-output time traces D_1, namely $\eta_1(k)$ and $y_1(k)$, are split into two parts, named D_{1_a} and D_{1_b}. Then, the data set D_{1_a} is used in order to identify an ARX model, M_{1_a}, which is finally validated against the data D_{1_b}. Similarly, M_{1_b} is identified by using D_{1_b}, and validated against D_{1_a}. This procedure is schematically shown in Fig. 7. The same approach is also repeated with D_2 and D_3, and, ultimately, six parametric models are identified and validated.

2) Second approach: An ARX model, M_1, is identified using the data set D_1, and validated against both D_2 and D_3. This approach is summarized in Fig 7. Finally, the same procedure is carried out by working with D_2 and D_3. Note that, in contrast to a traditional SI procedure, for this approach, the range of frequencies, and amplitudes, of the input signals employed in the validation phase is different from the range of frequencies, and amplitudes, over which the model is validated. Therefore, the second approach represents a cross-validation exercise where unsuitable training data are deliberately chosen and, as a consequence, poor validation performance is expected.

TABLE II
APPROACH 1 TRAINING

M_{1_a}	M_{1_b}	M_{2_a}	M_{2_b}	M_{3_a}	M_{3_b}
94.09	94.08	96.18	96.18	97.34	97.37

TABLE III
APPROACH 2 TRAINING

M_1	M_2	M_3
94.08	96.18	97.34

B. Model identification

Tables II and III report the percentage values of the fidelity of the models, defined as $100(1 - NRMSE)$, with respect to their corresponding identification data. These values remain, as expected, firmly consistent in relation to the data set employed for the identification. For instance, the fidelity of the models M_1, M_{1_a} and M_{1_b}, whose identification data are respectively D_1, D_{1_a} and D_{1_b}, is always about 94.08%. Moreover, it is interesting to note that the model fidelity reflects the signal-to-noise ratio of the identification data. Indeed, the experimental data D_3, which have the highest signal-to-noise-ratio, produces a model with the highest fidelity, namely M_3. This consideration becomes intuitive when the values in Table III are compared to the peaks of the spectra in Fig. 6.

C. Model validation

In the first approach, the parametric models are validated, by means of the 1-step-ahead, 5-step-ahead and 10-step-ahead predictions of the output, by using the corresponding validation data. For clarity sake, in a generic k-step-ahead prediction, the i-th output value is computed by using previously measured outputs up to time instant $i - k$ and relevant inputs up to time instant i. For instance, Fig. 8 compares the predicted output, $\hat{y}(t)$, of the model M_{3_b} to the measured output, $y(t)$, of the validation data D_{3_a}. Table IV reports the model fidelity with respect to validation data (VD), for the three types of output prediction. Note that the model performance remains consistent throughout the validation phase. First of all, the a-group and b-group of models always provide similar results. For instance, in the 5-step-ahead prediction of M_{2_a} and M_{2_b}, the model fidelity is, respectively, 84.82% and 85.57%. Secondly, the model fidelity unsurprisingly decreases as the number of steps ahead of the prediction increases. Finally, the fidelity of M_{1_a} (and M_{1_b}) is always the lowest, whereas the fidelity of M_{3_a} (and M_{3_b}) is the best in all cases.

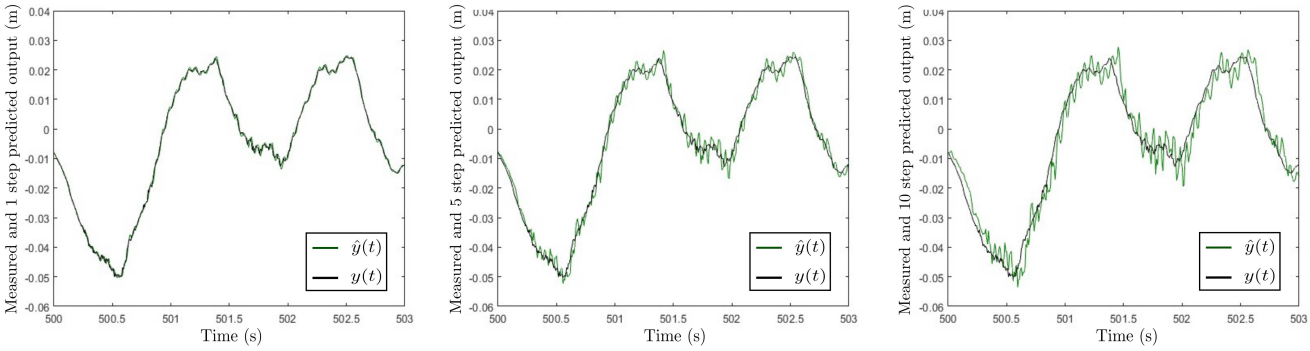

Fig. 8. From left to right, comparison between the measured output, $y(t)$, and the 1-step-ahead, 5-step-ahead and 10-step-ahead predicted output, $\hat{y}(t)$, related to the validation of model M_{3_b}.

TABLE IV
APPROACH 1 VALIDATION

Model	VD	1-step-ahead	5-step-ahead	10-step-ahead
M_{1_a}	D_{1_b}	93.91	81.69	60.46
M_{1_b}	D_{1_a}	93.91	81.69	59.91
M_{2_a}	D_{2_b}	95.93	84.82	67.90
M_{2_b}	D_{2_a}	95.92	85.57	69.27
M_{3_a}	D_{3_b}	97.32	92.49	84.41
M_{3_b}	D_{3_a}	97.33	92.60	84.76

TABLE V
APPROACH 2 VALIDATION

Model	D_1	D_2	D_3
M_1	-	87.44	91.71
M_2	84.01	-	92.74
M_3	83.82	87.14	-

Since the second approach is just a study case, only the 1-step-ahead prediction is employed for validation, and the model fidelity is reported in Table V. As expected, for the reasons already explained above, validation provides poorer results with respect to those of the 1-step-ahead prediction in Table IV and, furthermore, some unexpected outcomes are found. In particular, model M_2 validates better against data D_3 rather than against data D_1. However, in Fig. 6, since the frequency range of $S_2(f)$ basically overlaps the frequency range of $S_1(f)$, M_2 would be expected to validate better against D_1. A similar consideration can be given to model M_1, which performs better on D_3 rather than on D_2. Arguably, these unforeseen results may be explained by considering the signal-to-noise ratio of the data. Indeed, it is likely that the relatively low signal-to-noise ratio of D_1 and D_2 negatively affects the model validation performance. In any case, since the second approach is somewhat far from being the best practice in SI, and since investigating these results is not the main scope of this work, no further in-depth analysis has been conducted.

IV. Modelling in regular waves

A. Methodology

In the regular wave case, the identification method is focussed on the frequency domain, in order to derive some models of the transfer function (TF) of the system. In general, SI offers a wide range of modelling approaches in the frequency domain and, in particular, one of these methods consists of identifying a parametric model of the TF. In short, the input-output data of the system are used in order to derive the empirical frequency response function (FRF), namely the amplitude response and the phase response of the empirical transfer function, $H(j\omega)$. Then, a suitable parametric TF model and a criterion of fit are chosen, and, finally, the parameters are optimized on the basis of the fit criterion. However, the procedure adopted in this work is somewhat unusual because, since the time traces of the free surface elevation are missing, the empirical FRF is partially unknown.

Despite the incomplete knowledge of the input signals, thanks to the fact that the work is carried out for regular waves, it is still possible to find the empirical amplitude response, $|H(j\omega)|$. Indeed, in the regular wave case, the input is a simple sinusoid whose amplitude, A_w, and frequency, f, are known. Moreover, the displacement of the water column, i.e. the output signal, is also a sinusoid, whose frequency is equal to the input frequency. In other words, in the regular wave case, and for the specific model sought here, the input-output signals are sinusoids with the same frequency but possibly different amplitude. Therefore, $|H(j\omega)|$ is merely calculated as the ratio $A_\mathrm{OWC}/A_\mathrm{w}$, where A_OWC is the amplitude of the output. This ratio is computed for all the sixty input-output couples, and, ultimately, the points (circles) in Fig. 9 are found. As clarified by the use of different colors, these points are equally spilt, according to the input amplitude, into six separate sets of ten points each. Then, the ten points of each set are linearly interpolated, and six empirical amplitude responses, designated $|H_i(j\omega)|$, are obtained. Note that, in the case in which A_w = 5 mm, the amplitude response has a steeper trend with respect to that of the other cases. Arguably, this unrealistic behaviour of the system is solely due to the fact that, when the input amplitude is relatively small,

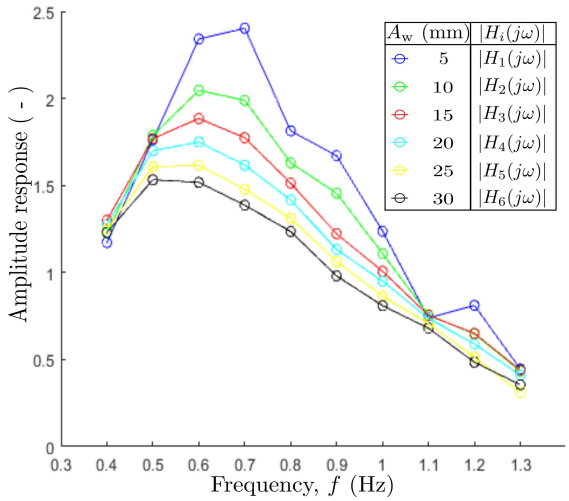

Fig. 9. Empirical amplitude response, $|H_i(j\omega)|$.

TABLE VI
ESTIMATION OF N_{z_i} AND N_{p_i}

$\hat{H}_i(j\omega)$	A_w (mm)	N_{z_i}	N_{p_i}
$\hat{H}_1$	5	7	14
$\hat{H}_2$	10	5	12
$\hat{H}_3$	15	5	10
$\hat{H}_4$	20	4	9
$\hat{H}_5$	25	3	10
$\hat{H}_6$	30	3	9

the output signal has a low signal-to-noise ratio and, as a consequence, the empirical measurements are noisy and not totally trustworthy.

In the remaining of this section, a modelling procedure is carried out as schematically shown in Fig. 10. This SI technique aims to find a family of TF models with consistent orders, by only relying on the empirical amplitude response as the identification data. As in the irregular wave case, the model performances are compared by using the NRMSE.

B. Rough models

In the first step of the identification procedure, a family of TF models with gains, g_i, poles, p_i, and zeros, z_i, has been chosen:

$$\hat{H}_i(j\omega) = g_i \frac{(z_i + j\omega)^{N_{z_i}}}{(p_i + j\omega)^{N_{p_i}}}, \quad i = 1, 2, \dots 6. \tag{5}$$

This particular TF model is adopted in order to roughly estimate the number of poles, N_{p_i}, and zeros, N_{z_i}, of the six transfer functions. In equation (5), g_i, p_i, z_i, N_{p_i} and N_{z_i} are all free parameters of the model, whose values are optimized by solving six separate data-fitting problems, in the least-squares sense. The main results are shown in Table VI, which reports the values of N_{z_i} and N_{p_i}.

C. Models with inconsistent orders

The estimates of N_{z_i} and N_{p_i} are utilized in order to define a second family of TF models, $\hat{H}_i^{'}(j\omega)$, which has the following form:

$$\hat{H}_i^{'}(j\omega) = g_i \frac{\prod_{n=1}^{N_{z_i}} (z_{i,n} - b_{i,n}(j\omega))}{\prod_{m=1}^{N_{p_i}} (p_{i,m} - d_{i,m}(j\omega))}, \quad i = 1, 2, \dots 6. \tag{6}$$

In equation (6), $z_{i,n}$ and $p_{i,m}$ are respectively the n-th zero and the m-th pole of the i-th transfer function, whereas, similarly, $b_{i,n}$ and $d_{i,m}$ are additional parameters of $\hat{H}_i^{'}(j\omega)$. As done in section IV-B, the free parameters of $\hat{H}_i^{'}(j\omega)$ are found by solving separate least-squares optimization problems and, ultimately, six TF models are identified. Table VII reports the model fidelity with respect to the identification data (ID), whereas Fig. 11 shows the comparison between the empirical data, $|H_i(j\omega)|$, and the model response, $|\hat{H}_i^{'}(j\omega)|$, for i = 1, 3, 6. Since N_{z_i} and N_{p_i} are not constant (Table VI), the TF models of this family are denoted as models with inconsistent orders.

TABLE VII
FIDELITY OF $\hat{H}_i^{'}(j\omega)$ AND $\hat{H}_i^{''}(j\omega)$

ID	A_w (mm)	$\hat{H}_i^{'}(j\omega)$	$\hat{H}_i^{''}(j\omega)$
$\|H_1(j\omega)\|$	5	96.38	87.39
$\|H_2(j\omega)\|$	10	99.35	97.95
$\|H_3(j\omega)\|$	15	99.84	99.74
$\|H_4(j\omega)\|$	20	99.82	99.80
$\|H_5(j\omega)\|$	25	99.47	99.46
$\|H_6(j\omega)\|$	30	99.68	99.68

D. Models with consistent orders

Since the identification data are gathered from the same OWC device, there is no particular *a-priori* reason why the orders of the TFs should change. Therefore, the final step of the identification procedure aims to find a family of models with consistent orders.

In order to equalize the TF orders, the number of zeros, and the number of poles, must be the same for all the six transfer functions. To this end, a suitable value for N_{z_i}, and N_{p_i}, may be chosen by calculating a sort of mean value:

$$N_z = \frac{\sum_{i=2}^{5} N_{z_i}}{5} = 4, \quad N_p = \frac{\sum_{i=2}^{5} N_{p_i}}{5} = 10. \tag{7}$$

Note that, in Table VI, the number of zeros, as well as the number of poles, does not vary much, with the only exceptions being N_{z_1} = 7 and N_{p_1} = 14. As already anticipated, these peculiar results are more likely due to the poor signal-to-noise ratio of the empirical measurements, rather than to the real behaviour of the system. This is the reason why, in equation (7), N_{z_1} and N_{p_1} are not taken into account.

The family of TF models with consistent orders, named $\hat{H}_i^{''}(j\omega)$, is trivially derived from equation (6) by imposing $N_{z_i} = N_z$ and $N_{p_i} = N_p$. As in the previous cases, the unknown parameters of the six transfer functions are determined by solving the corresponding least-squares optimization problems. The fidelity of the models is reported in Table VII, whereas Fig. 12 shows the comparison between the empirical data, $|H_i(j\omega)|$, and the model response, $|\hat{H}_i^{''}(j\omega)|$, for i = 1, 3, 6.

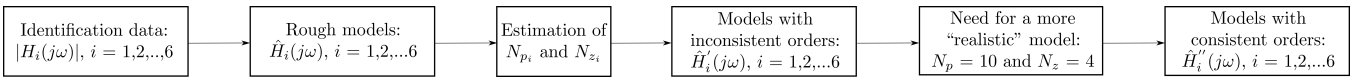

Fig. 10. Schematic representation of the modelling procedure in the regular wave case.

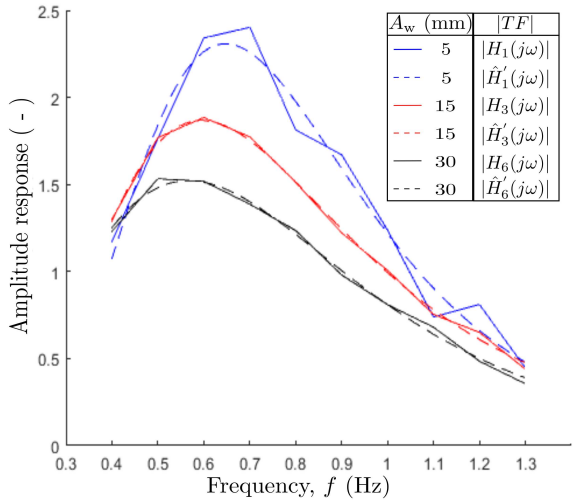

Fig. 11. Models with inconsistent orders: empirical amplitude response, $|H_i(j\omega)|$, and model amplitude response, $|\hat{H}_i^{'}(j\omega)|$.

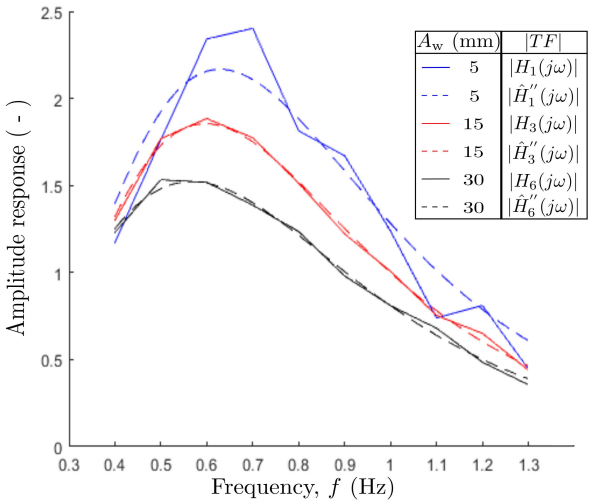

Fig. 12. Models with consistent orders: empirical amplitude response, $|H_i(j\omega)|$, and model amplitude response, $|\hat{H}_i^{''}(j\omega)|$.

E. Model performance evaluation

Table VII shows the comparison between the fidelity of the TF models $\hat{H}_i^{'}(j\omega)$ and $\hat{H}_i^{''}(j\omega)$. Despite the fact that the $\hat{H}_i^{'}(j\omega)$ models perform slightly better than the $\hat{H}_i^{''}(j\omega)$ model set, the performances of the two models is comparable in almost all cases. As expected, since N_{z_1} and N_{p_1} are not utilized in equation (7), the fidelity of the $\hat{H}_1^{'}(j\omega)$ and $\hat{H}_1^{''}(j\omega)$ models is notably different. However, for the reasons already explained above, this result has neither significant meaning nor real importance.

In order to provide more comprehensive insight into the outcomes of section IV, it is useful to focus on a single set of results, for instance the case A_w = 30 mm. First of all, Fig. 13 compares the empirical amplitude response to the amplitude response provided by $\hat{H}_6^{'}(j\omega)$ and $\hat{H}_6^{''}(j\omega)$, and, ultimately, it is almost impossible to appreciate any difference between $|\hat{H}_6^{'}(j\omega)|$ and $|\hat{H}_6^{''}(j\omega)|$. Secondly, in Fig. 14, the phase response of the model $\hat{H}_6^{''}(j\omega)$ is compared to the empirical phase response, calculated by using the data set D_3 for the irregular wave case. Since the empirical phase response is unknown in the regular wave case, this figure provides an alternative source of validation for the phase response. Finally, for the seek of completeness, Fig. 15 shows the pole/zero map for the transfer function $\hat{H}_6^{''}(j\omega)$.

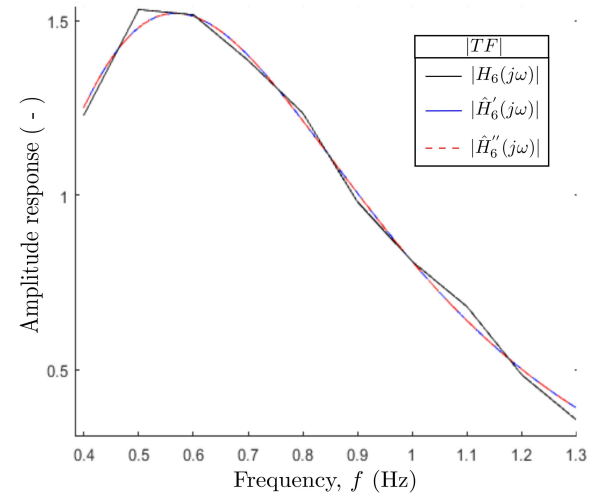

Fig. 13. Empirical amplitude response, $|H_6(j\omega)|$, and amplitude response of the models, $|\hat{H}_6^{'}(j\omega)|$ and $|\hat{H}_6^{''}(j\omega)|$.

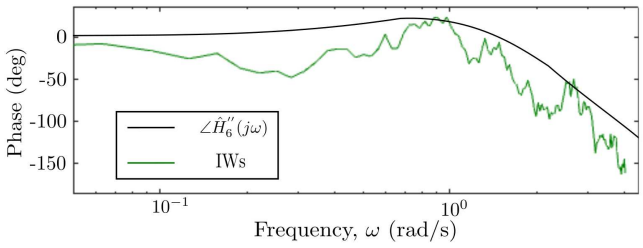

Fig. 14. Phase response of the model $\hat{H}_6^{''}(j\omega)$, and empirical phase response provided by the experimental data D_3 of the irregular wave case.

V. Model discussion

Despite the the fact that the ARX models, found in section III, and the models with consistent orders, identified in section IV, are derived from different sea state conditions (irregular and regular waves), it might be worth comparing the model orders. Ultimately, the number of poles (n_a = 4) and zeros (n_b = 2) of the ARX models is relatively small, especially when compared to the case of the models with consistent orders. As a

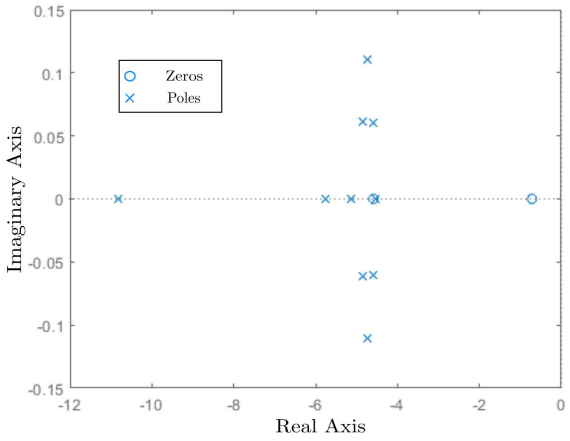

Fig. 15. Poles and zeros of $\hat{H}_6''(j\omega)$.

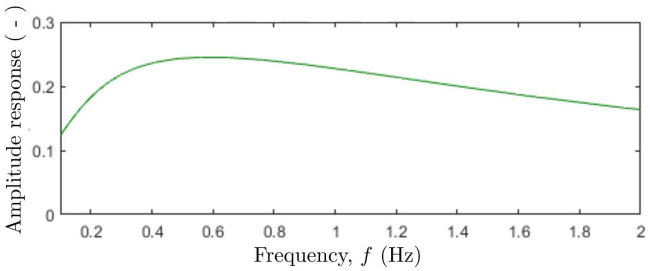

Fig. 16. Amplitude response of the ARX model M_{3_b}.

matter of fact, n_a and n_b are respectively smaller than N_p and N_z in equation (7).

Figure 16 shows the amplitude response of the ARX model M_{3_b}. The amplitude response of M_{3_b} is notably flatter and lower than the amplitude responses of the consistent models found for the regular waves (Fig. 12). Arguably, although this was not done for the current work, it may be possible to obtain the amplitude response of M_{3_b} with regular input signals. To this end, the range of regular frequencies, and regular amplitudes, should cover, up to a reasonable extent, the range of irregular frequencies, and irregular amplitudes, of the considered wave spectrum. For instance, the corresponding spectrum of model M_{3_b} is $S_3(f)$ (Fig. 6).

VI. Conclusion

In this work, data-based modelling techniques have been successfully employed in order to derive some wave-to-position models of an OWC device in IWs and RWs. In both cases, the results confirm that SI is able to provide accurate and simple models of OWC devices, providing that, during the experimental campaign, suitable input signals are chosen; otherwise, poor performance can be expected (Table V). The results in this paper correspond to a small-scale model operating in a controlled wave tank. However, believe the identification procedure can be extended to full-scale devices as follows:

- Full-scale devices can be simulated with high fidelity in, for example, CFD, which is an already established route to the determination of data-based parametric models [8].
- For ocean-based devices, an up-wave measurement, with a wave propagation model, is required to provide the input signal $u(k)$ in equation (3), using real irregular waves.

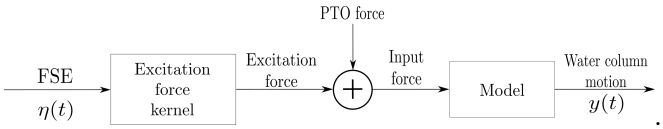

Fig. 17. Force-to-position model of a fixed OWC device.

The use of regular wave excitation for system identification, as documented in Section IV, is limited in ocean environments, unless the wave spectrum is narrow banded, approximating regular waves. However, even then, a selection of monochromatic (narrow banded) seas is required for complete identification of the system dynamics.

Despite the fact that this work does not focus on control strategies for OWCs, it is worth providing some consideration, since SI models may be potentially combined with data-driven control techniques in order to tackle the control problem of the PTO force. To this end, instead of considering a wave-to-position model (Fig. 3), a more comprehensive force-to-position model (Fig. 17), which includes the contribution of the PTO force and excitation force to the input force, could be adopted. Moreover, in order to keep a hypothetical control strategy relatively simple, it is important to refrain from using unnecessarily complex models. For instance, in relation to the outcomes reported in Table VII, the models with consistent orders should be preferred to the models with inconsistent orders.

In principle, for a given OWC device and deployment site, it may be possible to identify a linear ARX model for each of the most likely sea states, i.e. the sea states in which the device is expected to work. Such a modelling approach, which leads to a multi-linear ARX model, would require a switching/interpolation mechanism based on the sea state and, moreover, a method for estimating the sea state itself.

Finally, regarding real wave tank data gathering, there is still room for improvement. In particular, if the recorded data have a low signal-to-noise ratio, the model performance may be negatively affected (Table III), or the data may be severely corrupted by noise ($|H_1(j\omega)|$ in Fig. 9). Therefore, if waves with relatively small amplitudes need to be tested, the signal-to-noise ratio of the recorded data has to be improved.

References

[1] G. Mork, S. Barstow, A. Kabuth, and M. T. Pontes, "Assessing the global wave energy potential," in *International Conference on Offshore Mechanics and Arctic Engineering*, Shanghai, China, 2010, pp. 447–454.

[2] K. Gunn and C. Stock-Williams, "Quantifying the global wave power resource," *Renewable Energy*, vol. 44, pp. 296–304, 2012.

[3] B. Reguero, I. Losada, and F. Méndez, "A global wave power resource and its seasonal, interannual and long-term variability," *Applied Energy*, vol. 148, pp. 366–380, 2015.

[4] A. F. Falcão and J. C. Henriques, "Oscillating-water-column wave energy converters and air turbines: A review," *Renewable Energy*, vol. 85, pp. 1391–1424, 2016.
[5] L. Ljung, *System identification: Theory for the User*. Prentice Hall, 1999.
[6] L. Ljung, "Perspectives on system identification," *Annual Reviews in Control*, vol. 34, no. 1, pp. 1–12, 2010.
[7] J. Davidson, S. Giorgi, and J. V. Ringwood, "Identification of wave energy device models from numerical wave tank data—part 1: Numerical wave tank identification tests," *IEEE Transactions on Sustainable Energy*, vol. 7, no. 3, pp. 1012–1019, 2016.
[8] S. Giorgi, J. Davidson, and J. V. Ringwood, "Identification of wave energy device models from numerical wave tank data—part 2: Data-based model determination," *IEEE Transactions on Sustainable Energy*, vol. 7, no. 3, pp. 1020–1027, 2016.
[9] H. Cho, G. Bacelli, and R. G. Coe, "Linear and nonlinear system identification of a wave energy converter," Sandia National Lab.(SNL-NM), Albuquerque, NM (United States), 2018.
[10] F. Jaramillo-Lopez, B. Flannery, J. Murphy, and J. V. Ringwood, "Modelling of a three-body hinge-barge wave energy device using system identification techniques," *Energies*, vol. 13, no. 19, p. 5129, 2020.
[11] R. Gomes, J. Henriques, L. Gato, and A. Falcao, "Testing of a small-scale floating OWC model in a wave flume," in *International Conference on Ocean Energy*, Dublin, Ireland, 2012, pp. 1–7.
[12] T. Kelly, T. Dooley, and J. Ringwood, "Experimental determination of the hydrodynamic parameters of an OWC," in *Proceedings of the 12th European Wave and Tidal Energy Conference*, Cork, Ireland, 2017, pp. 1–10.
[13] T. Kelly, "Experimental and numerical modelling of a multiple oscillating water column structure," Ph.D. dissertation, National University of Ireland Maynooth, 2018.
[14] A. F. Falcão and J. C. Henriques, "The spring-like air compressibility effect in OWC wave energy converters: Hydro-, thermo-and aerodynamic analyses," in *International Conference on Offshore Mechanics and Arctic Engineering*. Madrid, Spain: American Society of Mechanical Engineers, 2018.
[15] S. Jacob, "Experimental and numerical modelling of an oscillating water column structure in irregular sea states," Master's thesis, Dundalk Institute of Technology, 2019.
[16] J. Falnes *et al.*, "Optimum control of oscillation of wave-energy converters," in *The Eleventh International Offshore and Polar Engineering Conference*. Stavanger, Norway: International Society of Offshore and Polar Engineers, 2001.
[17] J. Falnes, *Ocean Waves and Oscillating Systems*. Cambridge University Press, 2005.
[18] J. Rissanen, "Modeling by shortest data description," *Automatica*, vol. 14, no. 5, pp. 465–471, 1978.